Downscaling of daily topo-climatic variables within chestnut tree orchards in Lozère, France: temperatures, global radiations, potential evapotranspiration and precipitation

Valentine Delrieu, Florent Mouillot, Isabelle Chuine, Nicolas Ponsa, Yildiz Aumeeruddy-Thomas

Downscaling of daily topo-climatic variables within chestnut tree orchards in Lozère, France:

Temperatures, global radiations, potential evapotranspiration and precipitation

Valentine Delrieu, Florent Mouillot, Isabelle Chuine,
Nicolas Ponsa and Yildiz Aumeeruddy-Thomas

CEFE, Univ Montpellier, CNRS, EPHE, IRD (Montpellier, France)

Abstract:

Fine-scale climate projections are essential for anticipating the effects of climate change, which is critical for both agricultural resilience and biodiversity conservation. The ROC-CHÂ project, which focuses on the impacts of climate change on chestnut (*Castanea sativa* Mill.), developed this topo-climatic study in the aim of accurately model these global changes and their local impacts. The incorporation of topography into the modelling process is curcial, as terrain characteristics can generate microclimates, which may lead to significant variations in plant spatial distribution.

The modelling pipeline developed in this study was applied to a region in the Lozerian Cévennes (France) known for its numerous chestnut tree orchards. Combining empirical and machine learning approaches, this pipeline integrates topographical and meteorological inputs to produce 100-m resolution downscaled projections for the following climate variables: i) global solar radiation, and the associated weather variables of ii) minimum, maximum and mean temperatures, iii) potential evapotranspiration, and iv) precipitation. This modelling was carried out for both past (1990–2020) and future (2021–2100). For the historical period, observed weather station data were used, while for the future, the meteorological data used were based on simulations of the CNRM-CM5/ALADIN63 regional climate model applied to IPCC scenarios RCP 4.5 and RCP 8.5.

The resulting topo-climatic predictions can be visualized through maps, offering a powerful tool for participatory research with chestnut producers. These maps serve as a basis for dialogue and decision-making aimed at adapting agricultural practices to future climate conditions.

Key words: downscaling, topo-climate, chestnut orchards, Cévennes

Table of content

Introduction

Modelling plays a crucial role in anticipating the impacts of climate change on terrestrial ecosystems at both global and regional levels. At fine resolution, topography strongly influences microclimates, particularly in complex terrains where micro-topographic conditions make climate variables vary significantly (De Cáceres et al. 2018; Rita et al. 2021; Druel et al. 2025). Recent methods relying on machine learning have further enhanced topo-climatic downscaling by improving accuracy and adaptability (Rolnick et al. 2023; Bochenek and Ustrnul 2022). This improvement could also enhance the prediction of environmental responses to climate's future variations. In consequence, projections at fine resolution can help adapt agricultural practices to face upcoming climate changes. Combining robust topo-climatic simulations with biological mechanisms data (e.g., carbon acquisition, phenological processes) could for instance allow modelling species range shift with an increased accuracy (Chuine and Beaubien 2001; Lembrechts et al. 2019; Van Der Meersch et al. 2024).

Within this context, this work ultimately aims at improving our understanding of the impacts of climate change on chestnut agroecosystems in South-East France, which specifically grow in mountainous terrains. High-resolution topo-climatic downscaling is essential to accurately represent these local dynamics, that indeed have influenced the past management of these agroecosystem and is required today to guide on-going changes in climatic conditions.

A case study has been conducted in Lozère (France) in a mid-mountain area with high plateaux and valleys in the Lozerian Cévennes. This area is also known to harbour many chestnut tree orchards (Aumeeruddy-Thomas et al. 2012). The distribution of chestnut trees in the Euro-Mediterranean region is expected to be affected by climate change (Freitas et al. 2021; Álvarez-Álvarez et al. 2025). With the aim of predicting the shift range of chestnut trees in this area according to different climate change scenarios, a methodology has been developed to predict daily climate variables: i) global solar radiations, and the derived weather variables of ii) minimum, maximum and mean temperatures, iii) potential evapotranspiration, and iv) precipitation. The present report thus aims to describe the topo-climatic modelling chain allowing the computation of the selected climatic variables at fine resolution. The pipeline requires topographical and meteorological data, and computes the climatic variables with various computational methods, including machine learning-based approaches when deemed appropriate.

This work is part of the ROC-CHÂ project, a network for the *in situ* observation and conservation of chestnut varieties and associated traditional knowledge (Aumeeruddy-Thomas et al. 2024). In that context, the predicted topo-climatic variables can be represented on maps. These cartographic tools can then contribute to participatory approaches by facilitating result interpretation, discussions, and decision-making for a large audience (e.g., farmers, territorial institutions, etc.).

I. Input data

1. Digital elevation model

The first input needed is the **digital elevation model (DEM),** representing altitude as a grid in a GIS raster format at the chosen resolution. This file contains information about **elevation**, from which **slope** and **aspect** (i.e., North/South orientation) can be obtained within a GIS, and can be downloaded from various online databases. We downloaded the Advanced Spaceborne Thermal Emission and Reflection Radiometer Global Digital Elevation Model (ASTER-GDEM), released by NASA and Japan's Ministry of Economy, Trade and Industry. This DEM was recorded with 14 spectral bands (ranging from the visible to the thermal infrared wavelength region) and has a 30-meter resolution at the equator line (https://www.earthdata.nasa.gov/data/instruments/aster ; https://e4ftl01.cr.usgs.gov/ASTT/ASTGTM.003/2000.03.01/). From that global data, a large zone around the area's extent was selected in order to avoid deformation effects when modelling climate variables on the edges of the studied area.
In our case study, the area of interest covers 600 km^2, mainly located in the Lozère Administrative Department partly overlapping the Gard Administrative Department and the Cévennes national Park (see Appendix 1.a). The elevation of this area ranges from 106 m to 1700 m and the slope varies from 0 to 63°, making it quite a heterogeneous terrain. The area was largely covered by 35 ASTER-GDEM 8 by 8 km tiles, with an initial resolution of 25 m. All tiles have been put together and pixels have been aggregated in order to obtain one DEM file in 100 m resolution (see Appendix 1.b). This step was performed in R version 4.4.2 by using the function raster::aggregate() in RStudio, which attributes the mean value of the aggregated pixels. This aggregation at 100 m resolution was decided in order to reduce the computing time while still having a relevant resolution to interpret further model simulations for chestnut farms.

2. Meteorological data

The daily meteorological data used as inputs for topo-climatic downscaling are **minimum and maximum air temperature** in °C, solar radiation in W.m^{-2}, **wind speed** in m.s^{-1} and **precipitation** in mm. For France, these data can be freely retrieved from various sources: reference stations from Météo France (https://meteofrance.com) with a more or less dense network, gridded reanalysis of SAFRAN (https://www.umr-cnrm.fr/spip.php?article788) and ERA5-Land (https://cds.climate.copernicus.eu/datasets/reanalysis-era5-land) at 8 km and 0.1° resolution respectively. No finer resolution gridded information is available. Therefore, we also used data from a denser observation network that was installed at low cost for assessing the topo-climatic variability. Temperatures and wind speed have been downloaded for the 1990-2020 period from the **reference Météo France ground station** of Saint-Martin-de-Lansuscle (44°12'24'' N; 3°46'06'' E), which is located in the studied area at 643m elevation. In the valley around that station, a **temperature sampling campaign** was performed during the period 2013-2014 using temperature loggers (i-Buttons DS1923-F5, https://www.ibuttonlink.com) (Aumeeruddy-Thomas and Ramet 2020). Finally, precipitation data have been downloaded from the **SAFRAN database**. Table 1 shows the different sources of meteorological data and their use in this study.

<u>Table 1</u>: Sources of meteorological data used in this study.

	Reference station	**Field sampling**	**Gridded data**
Visual representation of data sources type Red dashed line: studied area		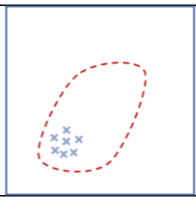	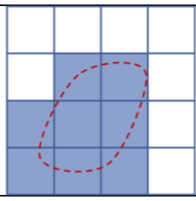
Historical data	Recorded by one reference ground station of Météo France located in the studied area	Recorded during a sampling campaign by i-Buttons data loggers in 2013-2014 at 27 locations around the reference station	SAFRAN grid
Future data	Extrapolation from DRIAS gridded data for the reference station location	/	DRIAS grid
Use	Model input	Model calibration	Model input for parameters that are not recorded by the reference station

Reference meteorological station: choice of time frame and handling of missing values

The historical time frame spans from 1990 to 2020 (i.e., 31 years which is sufficient to characterize a climate), allowing to capture the interannual variability and extreme events. We decided to start the modelling study in 1990, as it is after a turning point for the rise of temperatures in France (see Figure 1).

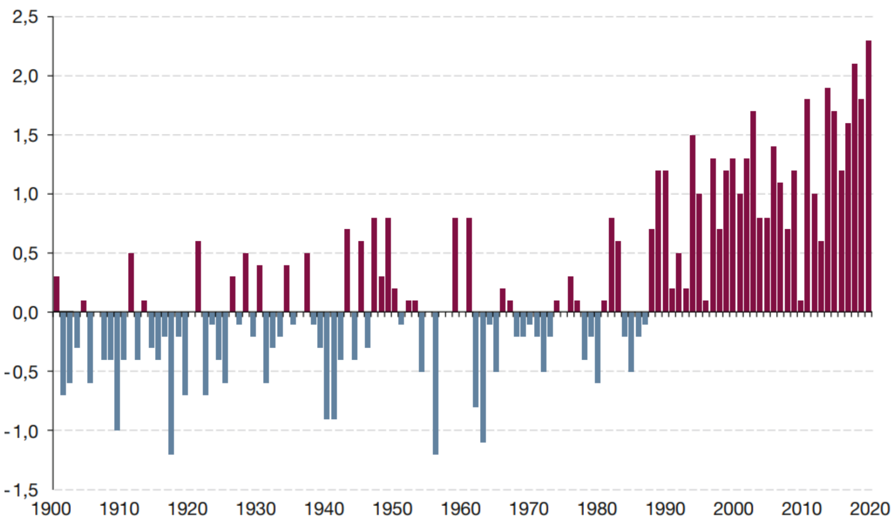

<u>Figure 1</u>: Deviation from normal mean annual temperature (°C) in continental France.

The change in mean annual temperature in 1900-2020 is shown as a deviation from the average observed over the period 1961-1990 (11.8°C). *Source:* (Baude et al. 2022)*(report from the French Ministry of ecological transition & the Service of data and statistical studies)*

Meteorological station data are rarely complete for the whole studied historical time period due to sensor failures or inconsistencies. For example, soil water content calculation requires previous-days soil water status, consequently failing in computing when one single data is missing. When **only one daily value** was missing, they were filled by **averaging** the values of the preceding and next days. However, to gap-fill for **larger periods** in the dataset, the data have been **extrapolated from another neighbouring reference station**. Sometimes, several back-up reference stations are needed but their number should be as limited as possible. The back-up station had to be located in the studied area, and of course it needed to have no common gap days with the reference station. The data recorded by all the meteorological stations of Lozère (code: 48) was downloaded from https://www.meteo.data.gouv.fr and data from the station **Saint-Martin-de-Lansuscle** was extracted. Two back-up stations were used for Saint-Martin-de-Lansuscle (SML): Mont-Aigoual Météo France station for extrapolations in the time frame 1990-2013 and Saint-Etienne for 2014-2020.
For each meteorological variable, a **qqplot** was created between the initial reference station (Y) and the back-up station (X), representing the quantile frequency correspondence of meteorological values between the two stations. Then, a **linear regression** was performed for each meteorological parameter. The coefficients of the established regression of the anomaly between both stations were finally used in order to produce extrapolated data for the initial reference station (Y). In turn, when a data is missing in Y, it is replaced by the value of Y-axis qqplot experiencing the same quantile frequency as the meteorological value of the same day in the X station (see Figure 2).

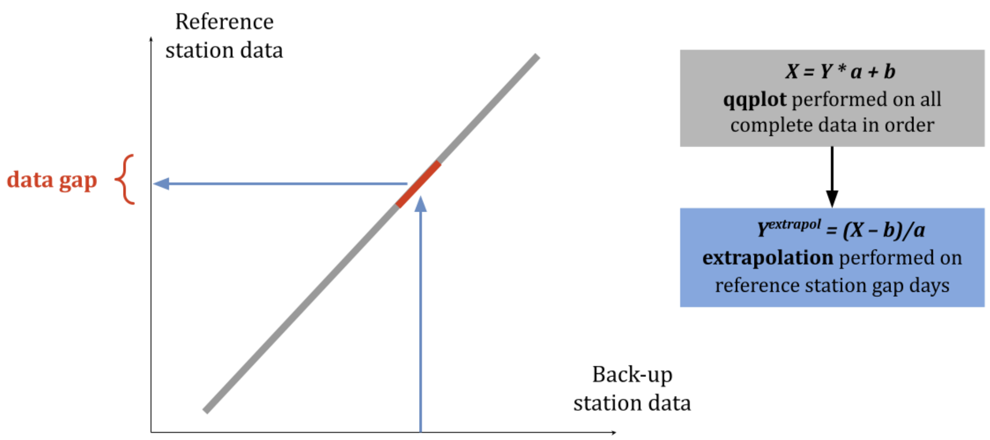

Figure 2: Linear regression for extrapolation of missing data in the reference station.

Field sampling methodology

Field sampling was performed between November 2012 and April 2014 on 27 locations in the SML's valley and at elevation ranging from 413 m to 867 m (see Figure 3). On each site, **minimum and maximum temperatures were recorded every 1 hour** by **iButtons** (DS1923-F5, https://www.ibuttonlink.com). In order to reduce biases in the recorded temperatures, each device was protected by a sunray shielding system (i.e., a white painted plant saucer) and installed at 1.80 m above ground in an area cleared from tree shade. This field sampling methodology is presented in greater details in (Aumeeruddy-Thomas and Ramet 2020).

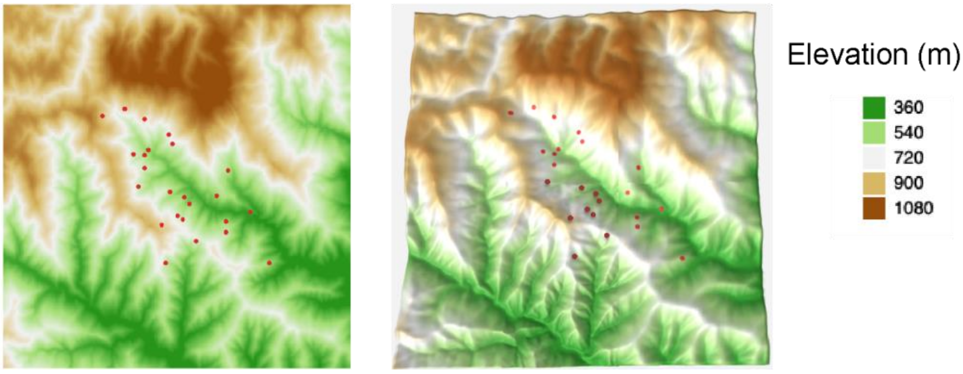

Figure 3: Map showing the 27 locations of the meteorological devices (red dots).

Source: D. Asse in 'Varietal diversity chestnut orchards and topo-climatic analyses in the Cevennes region' presented for the National Chestnut Group on Climate Change organised by the SNPC (National chestnut producers' union) in 24 June 2019.

SAFRAN data

SAFRAN (*Système d'Analyse Fournissant des Renseignements Adaptés à la Nivologie*) is a **meso-scale analysis of near-surface meteorological variables over France**, created by the French Meteorological Research National Centre (CNRM) and the Centre for Snow Studies (https://www.umr-cnrm.fr/spip.php?article788). Originally, it is a model for the evolution of the snow mantle, but it is commonly used as a source of complete meteorological data for physics-based models. Indeed, SAFRAN contains a **collection of recorded data** (e.g., temperatures, wind speed, near-surface humidity and precipitation) from various **observations, manual or automatic measurements**. These data can thus have general application for climate change studies. SAFRAN treats data by **dividing a limited domain into non-regular elementary zones**. The main constraint imposed on this zoning is a certain spatial homogeneity of the quantities analysed, making it more accurate on plain areas (Durand et al. 1993).
In this climate downscaling chain, data is retrieved from SAFRAN's **8 km resolution grids** for variables that are not recorded either during field sampling nor by the reference station, which is the case for precipitation. Daily precipitation was thus retrieved from SAFRAN over the studied area and the chosen historical time frame (i.e., 1990-2020).

DRIAS data

The time frame covered for projections goes from 2021 to 2100. The future meteorological data (i.e., minimum and maximum temperatures, wind speed and precipitation) have been downloaded **from DRIAS database** (https://www.drias-climat.fr). DRIAS data are formatted for an 8 km resolution grid. Because the DRIAS grid is based on the SAFRAN grid, no correction was applied between both datasets. The DRIAS data represent a mean value at an average altitude over a pixel. Since the altitude of the reference station differs from that of the centroid of the DRIAS and SAFRAN pixels, we corrected **the DRIAS data as follows**. For each meteorological variable, the anomaly between the value recorded at the reference station and the corresponding value of the SAFRAN pixel has been determined through linear regressions of qqplots. Anomalies were then applied to DRIAS data in order to obtain projected data for the reference station.

Climate data distributed by DRIAS are produced jointly by Météo-France IPSL, CERFACS, CNRM according to various **Representative Concentration Pathway (RCP) scenarios** and **climate**

models. RCP scenarios have been elaborated by the Intergovernmental Panel on Climate Change (IPCC) based on future greenhouse gases emissions. These scenarios are **based on radiative forcing**, which is linked to changes in many physical manifestations (in temperatures, air quality, sea levels, etc.). Remarkably, the manifestations of these climate change scenarios show **interannual/decadal variability** and are **not regionally uniform** (Calvin et al. 2023).

In the present case study, we selected two scenarios: **RCP 4.5** and **RCP 8.5** ("intermediate" and "very high" scenarios in Figure 4, respectively). On one hand, the **RCP 4.5 scenario** corresponds to a radiative forcing of about 4.5 W.m^{-2} and a concentration of about 660 ppm CO_2-equivalent at the stabilisation level after 2100, inducing a **stabilisation trajectory without overshoot**. In order for the climate to follow this scenario, great climate policies would be required, including major changes in the energy system (e.g., shifts to electricity and lower emissions energy technologies), and also in land use emissions allowing the expansion of forest lands (Thomson et al. 2011). This RCP 4.5 scenario is expected to limit global surface temperature change to a **2°C increase by 2100,** relatively to the average from the year 1850 to 1900 (Calvin et al. 2023). On the other hand, the **RCP 8.5 scenario** is associated to a radiative forcing greater to 8.5 W.m^{-2} and a concentration of about 1370 ppm CO_2-equivalent at the stabilisation level after 2100, meaning a **trajectory of increase, following current trend** (i.e., 'business as usual' scenario). It takes into account low rates of technological change and energy intensity improvements, while having a high growth in human population size and relatively slow increase in income (Riahi et al. 2011). Relatively to the average from the year 1850 to 1900, the global surface temperatures in this scenario are projected to increase by **more than 4°C in 2100** (Calvin et al. 2023).

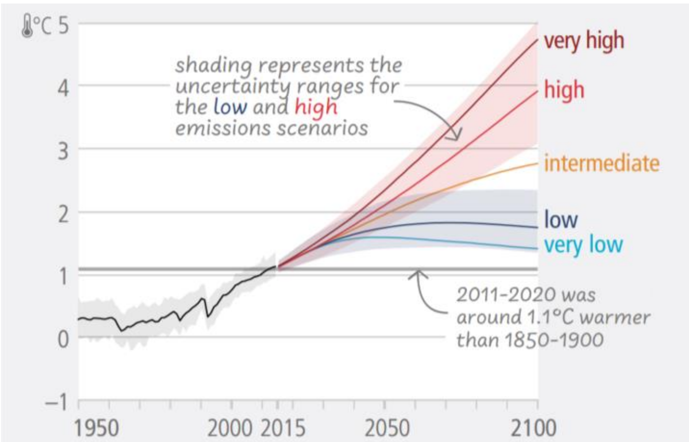

Figure 4: Global surface temperature change relative to 1850-1900 for IPCC scenarios.

Source: Calvin et al. 2023 *(IPCC AR6 report)*

Numerous climate predictive models are available on DRIAS, including regional and global ones. We have chosen the **CNRM-CM5/ALADIN63** climate model, which is the version 6.3 of ALADIN (*Aire Limitée Adaptation dynamique Développement InterNational*) created by the CNRM (https://www.umr-cnrm.fr/spip.php?article125). It is a **regional climate model**, which is better suited to fine scale analysis compared to global models. In particular, CNRM-CM5/ALADIN63 produces projections based on **atmospheric conditions** (i.e., temperature, pressure, humidity and wind speed), **surface parameters** (i.e., soil type and humidity, vegetal cover land use and topography), **ocean data** (i.e., sea surface temperature and sea ice cover) and **projections from global climate models**. This regional model relies on a **bi-spectral**, **semi-implicit**, **semi-Lagranian advection scheme**, meaning that the model uses two distinct spectral bands, computes atmospheric conditions from both current and future information, and that it performs both fixed grid interpolation and air particle movement analysis. As a result, projections have great precision and stability for long-term simulations (Nabat et al. 2020). In addition to its robust forecasting, the CNRM-CM5/ALADIN63 model has been selected because it is suited to France and produces rather median projections of temperature and precipitation change, in comparison to the projections of other models (see Figure 5).

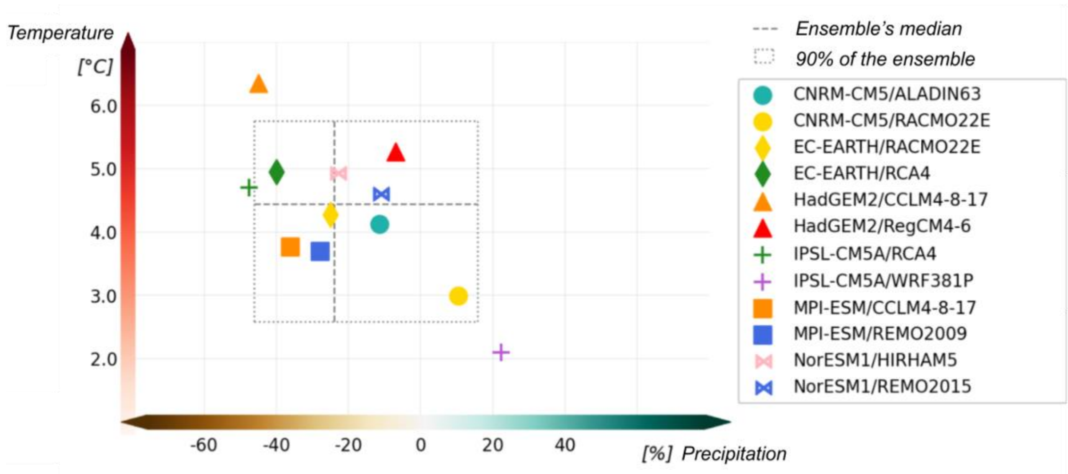

<u>Figure 5</u>: Scatterplot of individual simulations of the DRIAS-2020 ensemble.

Dispersion according to forecast changes in precipitation (x-axis) and temperature (y-axis) for the summer seasons at the end of the century according to the RCP 8.5 scenario. *Source: adapted from DRIAS*

II. Meteorological variables modelling and downscaling

The climate downscaling processing chain developed here ultimately aims at producing daily downscaled projections for i) **global solar radiations**, ii) **minimum, maximum and mean air temperatures**, iii) **potential evapotranspiration** and iv) **precipitation**. Some of these variables are also used as input in the calculations of others, shaping a processing pipeline (see Figure 6). Moreover, because of the **differences in nature and availability of each input meteorological data** (i.e., minimum and maximum temperature, wind speed and precipitation), different downscaling methods were applied R version 4.4.2 (see all RStudio packages in Appendix 2).

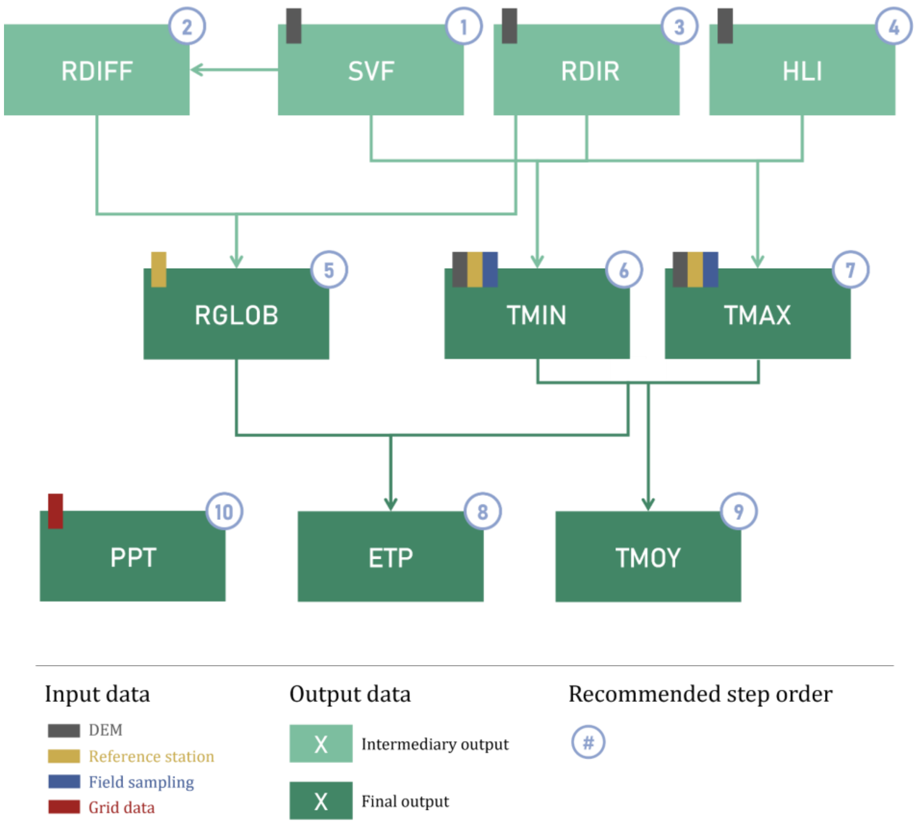

<u>Figure 6</u>: Climate variables computing process.

RDIFF; diffuse radiations; SVF: sky view factor; RDIR: direct radiations; HLI: heat load index; RGLOB: global radiations; TMIN: minimum temperature; TMAX: maximum temperature; PPT: precipitation; PET: potential evapotranspiration; TMOY: mean temperature.

1. Solar radiations

Skyview factor (SVF), direct radiations (RDIR, in J.m^{-2}) and Heat Load Index (HLI, in J.m^{-2}) and diffuse radiations (RDIFF, in J.m^{-2}) calculations were achieved through physics-based methods, using R CRAN packages 'RAtmophsere', 'oce' and 'insol' (see Appendix 2). All variables are computed based on the incoming solar rays' intensity across the seasons, and their angle of incidence on the terrain, thus only requiring the **Digital Elevation Model (DEM)** and coordinates of the zone (Druel et al. 2025).
Then RDIR and RDIFF were combined in order to compute the daily **global solar radiations (RGLOB, in MJ.m^{-2})**. However, this method only provides an estimation of RGLOB in theoretical clear sky condition. In order to account for nebulosity in RGLOB, minimum and maximum daily temperatures (TMIN and TMAX) are also used as inputs following the **Hargreaves equation** (Allen et al. 1998). These temperatures were recorded by the reference station for the historical period and DRIAS-extrapolated for the future period (see Figure 7).

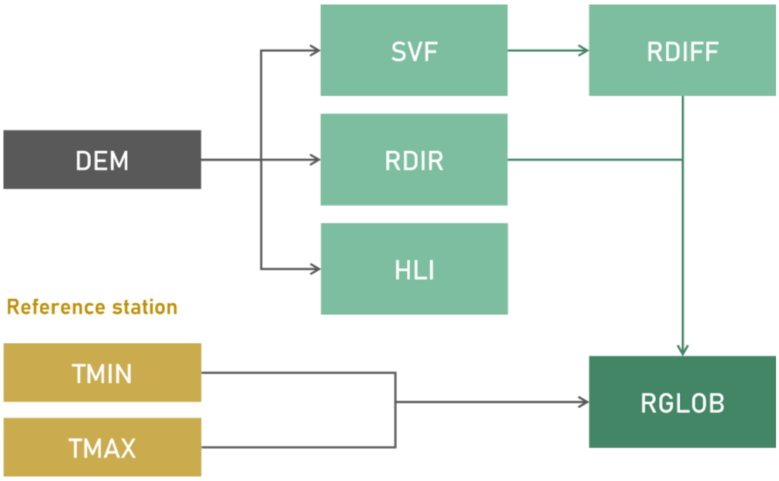

Figure 7: Solar radiations general modelling process.

DEM: digital elevation model; TMIN: minimum temperature; TMAX: maximum temperature; SVF: sky view factor; RDIR: direct radiations; HLI: heat load index; RDIFF; diffuse radiations; RGLOB: global radiations.

Skyview factor

The **skyview factor (*SVF*)** quantifies the proportion of sky openness at a given location, which influences the amount of diffuse solar radiation reaching a topographical location. This parameter **is strongly influenced by topographical factors**. For instance, high elevated areas (e.g., mountains) can cast shadow on lower ones, thus preventing direct radiations to hit some locations, which can locally lead to a lower temperature (Piedallu and Gégout 2008). Because interannual climate variations don't affect the SVF, it is computed for each day of the year (DOY), ranging from 1 to 365.
In the modelling process, the specificities of the study area are taken into account by **inputting coordinates and DEM tiles**. For each DOY, the SVF calculation consists in **simulating 1000 random sunrays**. For each simulation, the position of the sun, including azimuth (random direction in a 360° range) and elevation (random angle in a 90° range), is randomly selected using insol::SZA() and insol::sunAngle() respectively. A sun normal vector is then derived from these parameters. This **sun vector is computed along the DEM raster** by the insol::doshade() function in order to assess whether or not each pixel is reached by the sunray or intercepted by neighbouring hills, attributing a

value of 1 if reaching the pixel or 0 if intercepted (*sh*). After running the 1000 simulations, each pixel then can reach a value of 0 if none of the random sunrays could reach the pixel or 1000 if all the sun rays reach the pixel Finally, **the accumulated proportion of sky openness values over the entire day provides an estimate of the SVF, with a value rescaled between 0 and 1** (see Table 2).

$$SVF = \sum_{k=0}^{n} SVF_k \qquad \text{with } SVF_k = \frac{sh}{n} \text{ and } SVF_0 = 0$$

Table 2: Parameters used in the SVF calculation.

Symbol	Parameter	Equation or value	Unit
k	Current step of time fractions	From 0 to n	/
n	Total number of time fractions	201	/
SVF_k	Sky view factor at the kth step	Between 0 and 1	/
sh	Shadow (in the form of a raster file)	0 for shadow or 1 for light	/

Direct radiations, heat load index and diffuse radiations

The global radiations are split between a direct and a diffuse fraction. The first fraction refers to the proportion of light that directly reaches a point. These direct radiations are influenced by topography, relative sun position and atmospheric conditions (which is itself derived from the first two). The diffuse fraction of radiations has a lower access in valleys bottoms (i.e., bowl effect on diffuse radiations) in comparison with summits and plain area.

The modelling process of direct radiations (RDIR, in J.m^{-2}) requires the **DEM files and coordinates**. For each DOY, the model processes direct radiations by **simulating sun rays** throughout half-hourly fractions of the time frame going from sunrise to sunset. This time frame has been calculated each day according to latitude and day of year with the insol::suncalc() function). At each time step, the sun normal vector is derived from the DOY, time and coordinates through the function insol::SZA() for the sun zenith angle (sun elevation to horizon varying between 0° at sunset and sunrise and maximum angle at midday) and insol::sunAngle() for the sun azimuth (sun direction varying from East at sunrise to South at midday and west at sunset). Similarly to the SVF model, this sun vector and the DEM are used in the insol::doshade() function to obtain the **shading effect of surrounding hills**. A local **light intensity coefficient** is computed based on slope and aspect of each geographical point by the raster::hillShade() function. Combining both light intensity coefficient and shading effect allows a more accurate prediction of solar direct radiations in a complex terrain. These radiations are then computed as the product of shadow (*sh*), light intensity coefficient (*I*), sun parameters (i.e., solar constant (C_s) and ellipse factor of the Earth-Sun distance (*E*)) and atmospheric transmissivity (*T*) (see Table 3). Finally, **the accumulated amount of directly received light over the entire time frame provides an estimate of the daily direct radiation**.

The Heat Load Index (*HLI*) refers to the amount of direct radiations at the warmest period during the day. It is thus computed with the same method as direct radiations, but restricting the sun ray simulation time frame between 12pm and 2pm.

$$RDIR = \sum_{k=0}^{n} RDIR_k \quad \text{with } RDIR_k = sh * I * C_s * E * T * \Delta t \text{ and } RDIR_0 = 0$$

The model used for computing daily diffuse radiations (RDIFF in J.m^{-2}) is quite similar to the one used for direct radiations. However, it doesn't account for shade as, by definition, the direct impact of sun rays is not considered. The modelling process for diffuse radiations requires the **previously computed SVF as inputs, in addition to DEM and coordinates**. They are then computed with the *SVF* of the DOY corresponding to the computed date, sun parameters (C_s and E) and atmospheric transmissivity (T) (see Table 3).

$$RDIFF = \sum_{k=0}^{n} RDIFF_k \qquad \text{with } RDIFF_k = SVF * I * C_s * E * T * \Delta t \text{ and } RDIFF_0 = 0$$

<u>Table 3</u>: Parameters used in the direct and diffuse radiations calculation. (Kumar et al. 1997)

Symbol	Parameter	Equation or value	Unit
a0	Initial transmission coefficient	$0.4237 - 0.00821 * \left(6 - \left(\frac{elevation}{1000}\right)\right)^2$	/
a1	Supplementary attenuation coefficient	$0.5055 - 0.00595 * \left(6.5 - \left(\frac{elevation}{1000}\right)\right)^2$	/
C_s	Solar constant	1369	W.m^{-2}
Δt	Length of a time fraction	$\frac{t_{sunset} - t_{sunrise}}{n}$	s
E	Ellipse factor for Earth-Sun distance	$1 + 0.033 * cos\left(\frac{2 * \pi}{365}\right)$	/
ext	Extinction coefficient	$0.2711 - 0.01858 * \left(2.5 - \left(\frac{elevation}{1000}\right)\right)^2$	/
I	Light intensity coefficient	Included between 0 and 1	/
k	Current step of time fractions	From 0 to *n*	/
n	Total number of time fractions	201 in case study	/
$RDIR_k$	Direct radiations at the k^th^ step	/	W.m^{-2}
$RDIFF_k$	diffuse radiations at the k^th^ step	/	W.m^{-2}
SVF	Sky view factor	*previously computed*	/
T	Atmospheric transmissivity	$a_0 + a_1 * e^{-\frac{ext}{cos(\theta)}}$	/
θ	Solar zenith angle	$90 - \frac{solar\ angle * \pi}{180}$	°

Global radiations

Once the direct and diffuse radiations are obtained, the daily global radiations (RGLOB, in MJ.m^{-2}) can be computed by adding the diffuse and direct radiations, modified by the nebulosity index sharing diffuse and direct radiation differently. We first estimated the nebulosity by the Hargreaves method (George H. Hargreaves and Zohrab A. Samani 1985; *HEC-HMS Technical Reference Manual*, n.d.). The fraction of diffuse and direct radiation according to nebulosity (Roderick 1999), with the difference between *TMAX* and *TMIN* shown to be a proxy of cloud cover. In this formula, daily minimum and maximum temperatures recorded by the reference station are taken into account in the calculation of the fraction of total radiations (*ftot*) (see Table 4). Global radiations are thus computed for every day covered in the study (e.g., 11,323 days for the time period of 1990-2020).

$$RGLOB = ftot * 1 - fdiff * RDIR * [fdiff * RDIFF]$$

<u>Table 4</u>: Parameters used in the Hargreaves formula.

Symbol	Parameter	Equation or value	Unit
a	coefficient correcting the fact that transmittance is taken into account both in K_H and *RDIR*	1.6 so that *ftot*=1 when *TMAX*–*TMIN*=15	/
fdiff	fraction of diffuse radiations	$\frac{RDIFF}{RDIR + RDIFF}$	/
ftot	fraction of total radiations	$K_H * \sqrt{TMAX - TMIN} * a$	/
K_H	Hargreaves shortwave coefficient	0.17 default value 0.16 for interior areas 0.19 for coastal areas	/

2. Temperatures

Topographical variations in daily air temperatures were assessed with a **Random Forest (RF)** relating temperature anomalies between the reference station and field sampling according to their explanatory variables. This process allows for assessing the non-linear and interacting influences of several topographical and daily climatic parameters on local temperature variations. In this aim, R CRAN packages 'randomForest', and 'grf'.
Once calibrated, the RF models (i.e., one for minimum temperature and another one for maximum temperature) are used with the reference station data in order to produce projections for both historical and future time periods. Then, mean temperature can be inferred from minimum and maximum temperatures (see Figure 8).

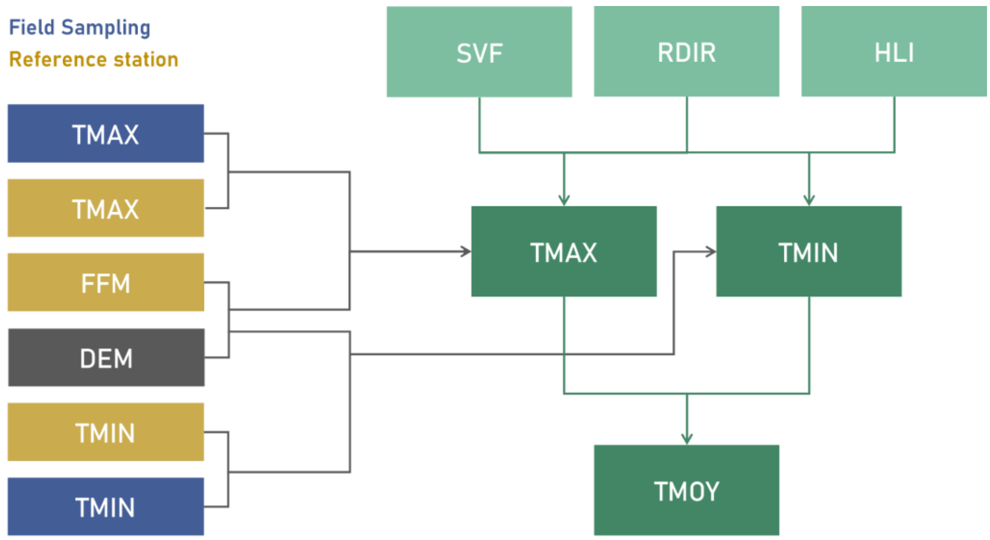

Figure 8: Temperatures general modelling process.

TMAX: maximum temperature; FFM: wind speed; DEM: digital elevation model; TMIN: minimum temperature; SVF: sky view factor; RDIR: direct radiations; HLI: heat load index; TMOY: mean temperature.

Minimum and maximum daily temperature

RF is an ensemble learning method consisting of three main steps: i) building multiple decision trees, ii) bagging (i.e., bootstrap aggregating), and iii) results aggregation. It can be used both for classification, by returning the most frequent prediction, and for regression, by returning the average prediction. Each tree is trained on a random subset of the data and features, which increases diversity and reduces the risk of incorporating too much detail or specific noise from training data, leading to inaccurate predictions on new data (i.e., overfitting) (Rigatti 2017). This method is particularly effective in handling datasets with high dimensionality and interactions among variables (Sekulić et al. 2020).
Here, the field sampling data are used to calibrate the model and to select the best fitted RF model explaining the variation between air temperatures recorded by field sampling and reference station in ($T_{Sampling} \sim T_{Reference}$). Remarkably, the elevation range of the field sampling was restricted to a certain elevation range (between 413 m and 867 m for the SML valley), meaning that some extreme elevations in the studied area would not be handled well by a classical RF model, using the function randomForest::randomForest(). For that reason, a local linear RF model was used through the

grf::ll_regression_forest() function with default parameters. This approach is based on a non-parametric regression and offers better flexibility and robustness when simulating data (Friedberg et al. 2021). For both **minimum and maximum temperature (TMIN and TMAX, respectively, both in °C)**, several variables have been tested (see Table 5) in order to obtain the best fitted model. Then, following the hypothesis that the relationship established in the SML valley can be applied to a larger extent, the resulting model is applied to the whole studied area.

Table 5: tested variables for explaining temperature variations.

Variables	Sources
Elevation	extracted from DEM
Aspect	extracted from DEM
Slope	extracted from DEM
Skyview factor	previously computed
Nebulosity	approximated with $\sqrt{TMAX - TMIN}$
Direct radiations	previously computed direct radiations (in clear sky conditions)
Heat Load Index	previously computed similarly to direct solar radiation, except that sun rays are only simulated between 12pm to 2pm
Reference minimum/ maximum temperature	Reference station
Wind speed	Reference station

In this study, the best fitted model found for minimum temperature variation was obtained with 2000 trees using 12067 training samples. This model explained 59.2% of the variation, with a root-mean-squared error (RMSE) of 0.57. This last indicator means that the projected minimum temperatures have an error margin of ±0.57°C. From most to least influential, it includes the effects of **elevation** (65.8% of explained variation), **skyview factor** (17.0% of explained variation), **wind speed** (8.8% of explained variation), **reference minimum temperature** (5.5% of explained variation) and **nebulosity** (2.9% of explained variation).
The best fitted model for maximum temperature variation was obtained with 2000 trees using 10932 training samples. This model explained 57.4% of the variation, with a RMSE 0.59°C. From most to least influential, it includes the effects of **elevation** (71.4% of explained variation), **aspect** (12.9% of explained variation), **slope** (5.0% of explained variation), **wind speed** (3.8% of explained variation), **nebulosity** (3.3% of explained variation), **direct radiations** (2.5% of explained variation) and **reference maximum temperature** (1.2% of explained variation).

Daily mean temperature

The daily **mean air temperature (TMOY, in °C)** is computed as the **arithmetic mean value of minimum and maximum daily temperatures**. This simple method allows to approximate daily mean temperature without needing hourly temperature data. Given the margin of error for both minimum and maximum temperature (±0.57°C and ±0.59°C, respectively), mean temperature is obtained with a ±0.58°C margin of error.

3. Potential evapotranspiration

Evapotranspiration represents the loss of water both through plant transpiration (*via* vascular system) and evaporation of water from the earth's surface. Potential evapotranspiration corresponds to the evapotranspiration calculated according to climatic demands for a dense lawn on soil saturated with water. This variable can be influenced by several factors such as temperature, humidity and sunlight. There are several methods allowing to compute **daily potential evapotranspiration (ETP, in mm)**. Among them, the Priestley-Taylor method is a mechanistic approach that is widely used for estimating regional potential evapotranspiration (Allen et al. 1998; Anupoju et al. 2024). Here, a **simplified Priestley-Taylor method** is adopted in order to compute daily potential evapotranspiration solely from global radiations, minimum and maximum temperatures as inputs (see Figure 9).

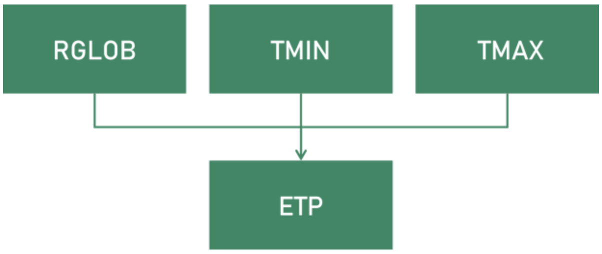

Figure 9: Potential evapotranspiration general modelling process.

RGLOB: global radiations; TMIN: minimum temperature; TMAX: maximum temperature; PET: potential evapotranspiration

The original Priestley-Taylor method computes potential evapotranspiration as shown in the equation (1), where R_n is the net radiations and G is soil heat flux density, both in MJ.m^{-2} (Priestley and Taylor 1972). This equation has been adapted by considering that G is negligible and dividing R_n with the volumetric latent heat flux of vaporization in MJ.m^{-3} (lv) (see Table 6). This step allows the conversion of energy in Joules to the height of evaporated water in millimetres, see equation (2).

$$PET = \alpha_b * \frac{\Delta}{\Delta+\gamma} * (Rn - G) * 10^3 \quad (1)$$

$$PET = \alpha_b * \frac{\Delta}{\Delta+\gamma} * \frac{Rn}{lv} * 10^3 \quad (2)$$

with $\Delta = \frac{4098 * es}{(TMAX+237.3)^2}$; $\gamma = \frac{Cp * P}{lm * \frac{Ra}{Rv}}$; $Cp = \left(1.005 + 1.82 * \frac{\frac{Ra}{Rv} * ea}{P - ea}\right) * 10^{-3}$

The actual vapour pressure in kPa (ea) is computed using the saturation vapour pressure in kPa (es) and the relative humidity (RH). However, when one of these last two data is not available, the ea can be derived from another formula, only relying on the temperature at dew point. In this case study, neither relative humidity or dew point temperature is available. However dew point temperature can be approximated using minimum temperature (Allen et al. 1998), as shown in the equations hereafter. This final simplification enables the computing of daily potential evapotranspiration based solely on **previously obtained daily global radiations, maximum and minimum temperatures** (see Table 6).

$$ea = es * RH$$

$$ea = 0.611 * exp^{\frac{17.27 * (Tdew-1)}{Tdew-1+237.3}}$$

<u>Table 6</u>: Parameters used in the Priestley-Taylor formula.

Symbol	Parameter	Value or equation	Unit
α_b	Priestley-Taylor coefficient	1.26	/
albedo	albedo (i.e., fraction of light reflected by the surface)	0.15	/
Cp	Mass heat of the air at a constant pressure	$\left(1.005 + 1.82 * \frac{\frac{Ra}{Rv} * ea}{P - ea}\right) * 10^{-3}$	kPa.kg^{-1}.°C^{-1}
Δ	Slope of the vapour pressure curve	$\frac{4098 * es}{(TMAX + 237.3)^2}$	kPa.°C^{-1}
ea	Actual vapour pressure	*es*RH* or $0.611 * exp^{\frac{17.27 * (Tdew-1)}{Tdew-1+237.3}}$	kPa
es	Saturation vapour pressure	$(1.0007 + 3.46 * 10^5 * P) * 6.1121 * exp^{\frac{17.502*TMAX}{240.97+TMAX}}$	kPa
γ	Psychrometric constant	$\frac{Cp * P}{lm * \frac{Ra}{Rv}}$	kPa.°C^{-1}
lm	Latent heat of vaporization for a mass	2.453	MJ.kg^{-1}
lv	Volumetric latent heat flux of vaporization	2453	MJ.m^{-3}
P	Atmospheric pressure	101.325	kPa
Ra	Gas constant of dry air	286.9	J.kg^{-1}.K^{-1}
RH	Relative humidity	*Not available*	/
RGLOB	Daily global radiation	*Previously computed*	MJ.m^{-2}
Rn	Daily net radiation	*RGLOB * albedo*	MJ.m^{-2}
Rv	Gas constant of vapor pressure	461.5	J.kg^{-1}.K^{-1}
Tdew	Daily temperature at dew point	*Approximated with TMIN*	°C
TMAX	Daily maximum temperature	*Previously computed*	°C
TMIN	Daily minimum temperature	*Previously computed*	°C

4. Precipitation

Finally, the downscaling of **daily precipitation (PPT, in mm)** is performed differently because previous meteorological parameters and topography cannot explain enough of the rainfall variations. Moreover, precipitation is only available on gridded data, conversely to the previous parameters. The **gridded precipitation data** has been retrieved from **SAFRAN** and **DRIAS databases**. More specifically to precipitation, the version 6.3 of the ALADIN model includes convection, moist turbulence and large-scale microphysics schemes, which enables the description of rainfall (Nabat et al. 2020). Additionally, the land surface is simulated using a two-way system coupling the Interaction Soil Biosphere Atmosphere and the CNRM version of Total Runoff Integrating Pathways (ISBA-CTRIP). Among other parameters, this system allows the model to represent precipitation interception (Decharme et al. 2019).

No precipitation data was recorded either by field sampling or by the reference meteorological station. Moreover, **topographical parameters have a negligible influence** on the amount of daily rainfall. The precipitation parameter has thus simply been downscaled to a 100 m resolution from the SAFRAN or DRIAS grid (for historical or future time period, respectively), both initially at an 8 km resolution. This downscaling was performed by **resampling with a simple bilinear model** with function raster::projectRaster(). This method computes the **distance-weighted average of the four nearest neighbours** around the target pixel. This process is performed both in horizontal and vertical directions, thus making this method 'bilinear'. Finally, if a pixel gets any negative prediction precipitation, the value 0 is attributed.

III. Application example: topo-climatic mapping of mean temperatures

The modelling pipeline described above produces daily predictions of topo-climatic variables in a .tif format, which means that **they can be visualized as maps** on GIS software. However, these day-by-day predictions cannot be used as such because of the uncertainty associated with the models and the daily climate variations.
Therefore, **daily data need to be averaged over several decades** in order to produce a robust interpretation. In this study three 25-years-periods were chosen: 2026-2050, 2051-2075 and 2076-2100. Moreover, data were **sorted by season** in order to avoid a smoothing effect due to seasonal variations. Indeed, averaging for instance all daily maximum temperature data over several years would conceal the observed differences of temperatures in winter and summer. Remarkably, the seasonal breakdown used in this study was based on periods linked to strategic phenological stages of the chestnut tree, rather than the standard distinction between seasons. As a result, spring consisted of the months of March, April, May and June, summer was July and August, autumn was September, October and November, and finally winter was associated with December, January and February. Daily prediction files were thus first sorted according to the corresponding combination of variable, RCP scenario, season and time period (e.g., mean temperatures predicted according to the RCP 4.5 scenario for summers between 2026 and 2050). Then, for each combination, all daily files were averaged in order to finally obtain a single .tif file, in which each pixel is associated with the local average value.

Additionally, if an indicator for the main trend is needed, **the value of each pixel in the obtained .tif file can also be averaged**. This results in a single value corresponding to the average variable across both the area and time period. Though this method hides some of the intra-area variability, it allows for a **global view of the overall trends** shown in the predictions. For instance, given the description of the chosen scenarios, the predicted mean temperatures are expected to stabilize in RCP 4.5 and to keep increasing in RCP 8.5, which is what has been observed in this case study (see example of the period-and-area-averaged summer mean temperatures in Table 7).

Table 7: Predicted summer mean temperatures averaged across the whole studied area and over 25 years periods of time

IPCC scenario	Time period	Average summer Tmean of the area (°C)	sd
RCP 4.5	2026-2050	22.1	1.5
RCP 4.5	2051-2075	22.7	1.4
RCP 4.5	2076-2100	22.8	1.3
RCP 8.5	2026-2050	21.7	1.3
RCP 8.5	2051-2075	23.5	1.5
RCP 8.5	2076-2100	25.5	1.4

Cartography then allows us to further refine the interpretation, especially accounting for local variations due to topographical specificities. For instance, the period-averaged summer mean temperatures (Figure 10 and 11) show a significant impact of scenario and topography on temperature changes.

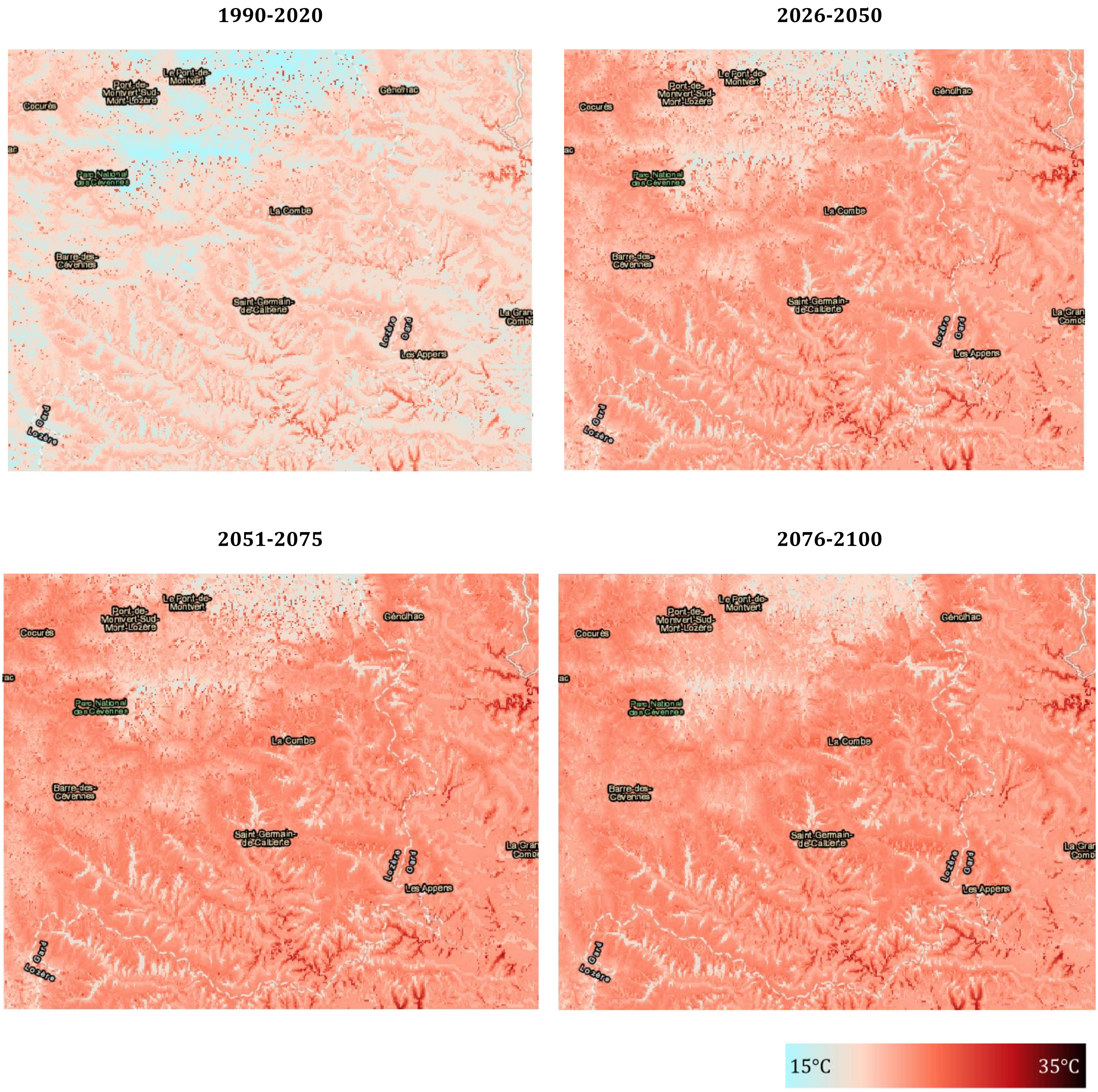

Figure 10: 100 m resolution maps of the studied area representing the summer mean temperatures averaged over 25 years periods*, following the RCP 4.5 scenario (stabilization trajectory).

*The first map shown was not obtained with the scenarios, as it is based on the past temperatures recorded between 1990-2020 (i.e., 30 years period) and serves as a reference point.

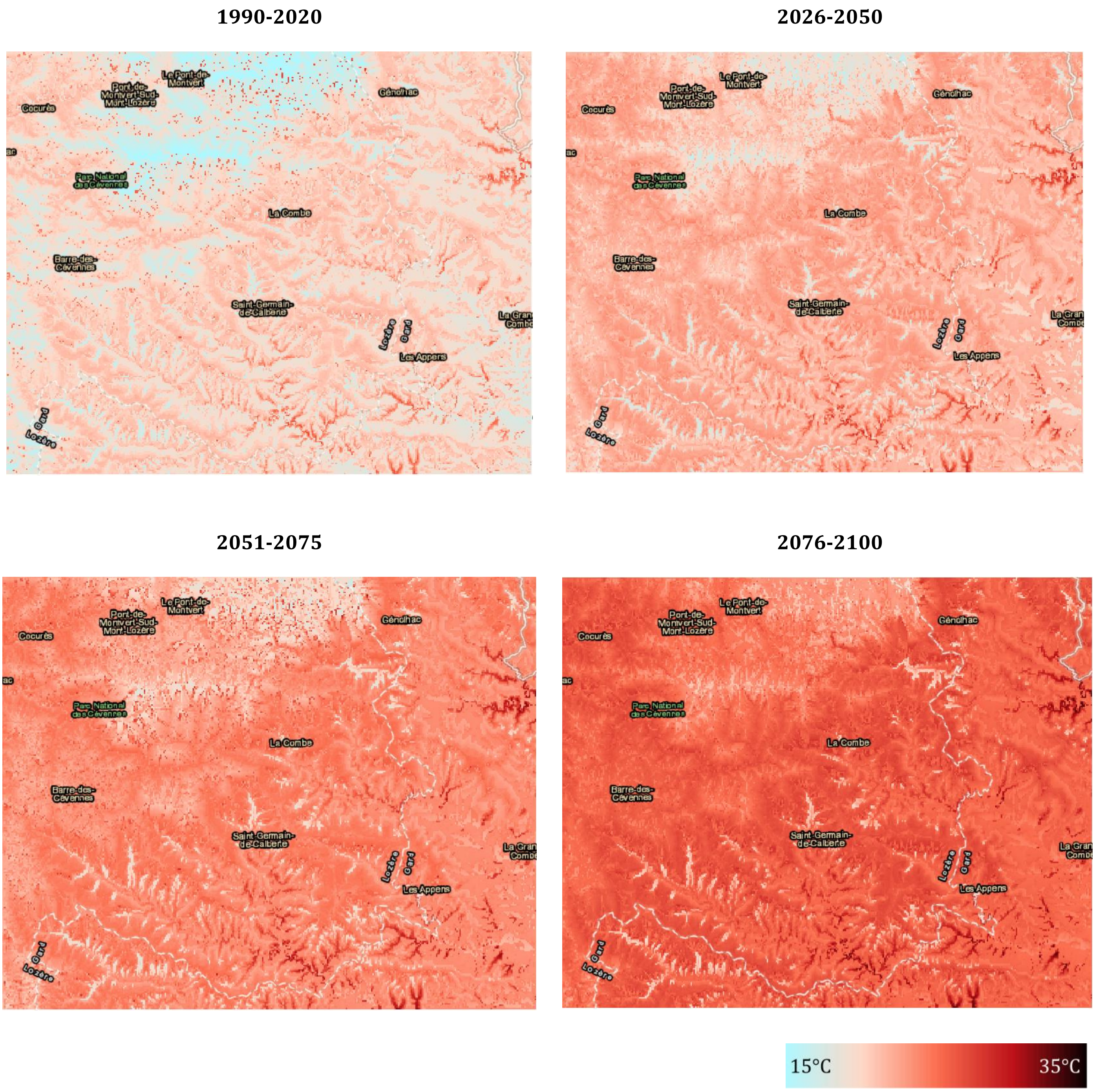

<u>Figure 11</u>: 100 m resolution maps of the studied area representing the summer mean temperatures averaged over 25 years periods*, following the RCP 8.5 scenario (increase trajectory).

*The first map shown was not obtained with the scenarios, as it is based on the past temperatures recorded between 1990-2020 (i.e., 30 years period) and serves as a reference point.

Discussion

The aim of the modelling pipeline described here is to obtain the following downscaled key topo-climatic parameters in areas used for chestnut production: solar radiations, air temperatures, potential evapotranspiration and precipitation. The computing methods employed here were based on the available data of a 600 km² area in Lozère (France).

Regional climate model: CNRM-CM5/ALADIN63

The DRIAS projection climate data used as input in this process (i.e., wind, temperatures and precipitation simulations) were based on the CNRM-CM5/ALADIN63 regional climate model (RCM). This model was chosen because it produces median projections and because it includes an evolutive radiative forcing. Indeed, thanks to political measures aiming at limiting atmospheric pollution, a strong decrease in anthropic aerosols emissions since the 1980s has occurred. This phenomenon has resulted in an increase of the direct radiation in the Euro-Mediterranean region (Nabat et al. 2014), which is taken into account in CNRM-CM5/ALADIN63.
The CNRM-CM5/ALADIN63 model, average windspeed simulation shows a bias smaller than ±1m/s in comparison to SAFRAN data, which is relatively low compared to the other RCM from the European Coordinated Regional Downscaling Experiment (EURO-CORDEX ; Jacob et al. 2020) initiative (Robin et al. 2023; Vautard et al. 2021). As a result, CNRM-CM5/ALADIN63 is a rather good model for wind and radiation.
However, the model has been shown to carry a negative bias for temperatures (i.e. greater than -2°C in a large part of France) and a positive bias for precipitation (i.e. increase of 15% in a large part of France, and greater than 50% locally). The observed temperature and precipitation biases are heterogeneously distributed across seasons. For instance, the bias in temperature simulation is only -0.5°C in winter and the bias in precipitation simulation is more than 100% in summer. Regardless of seasons, these biases (i.e., temperature underestimation and precipitation overestimation) are exacerbated in mountainous areas (Robin et al. 2023). Both these biases found in the CNRM-CM5/ALADIN63 model are consistent throughout most other EURO-CORDEX RCM (Vautard et al. 2021).
In consequence, the simulations obtained in this study with CNRM-CM5/ALADIN63 tend to underestimate temperature and overestimate precipitations. The prediction of these variables could be sharpened through corrections. For instance, the Explore 2 report (2025) assesses four different correction methods: ADAMONT (quantile mapping correction applied conditionally to time regimes; (Verfaillie et al. 2017), CDF-*t* (Cumulative Density Function transfer; (Michelangeli et al. 2009), R2D2 (analogue Rank Resampling for Distributions and Dependences; (Vrac and Thao 2020; Vrac 2018) in version 0L (i.e., without taking time into account) or version 2L (i.e., conservation of 3 days sequences). CDF-*t*, R2D2 0L and R2D2 2L are able to correct the bias of each variable separately. Both R2D2 methods add a correction to the inter-variable dependence structure, but they also degrade the spatial structure. The ADAMONT method allows to maintain inter-variable spatial and temporal structures despite slight residual biases remaining (Robin et al. 2023).

Solar radiations

The global solar radiation modelling method used in this study is based on (Kumar et al. 1997), which includes the empirical method (George H. Hargreaves and Zohrab A. Samani 1985). It relies on diffuse and direct radiation, as well as minimum and maximum temperatures recorded in the reference station. However, this method does not inherently include the impact of topography. In

consequence, in order to account for the terrain characteristics of the studied area, the sky view factor and the shading effect have been included in the calculation of diffuse and direct radiations, respectively (Piedallu and Gégout 2008; Druel et al. 2025). For that purpose, both these fractions of the global radiations were computed with the digital elevation model of the area.
Many other methods exist for global solar radiation modelling (i.e., empirical models, time series, artificial intelligence or hybrid models). However, each model has its own advantages and disadvantages, and their performance is found to be context-dependent. Hybrid models tend to be slightly more reliable and accurate, but the computational cost associated is much higher than that of empirical models (Gürel et al. 2023).

Air temperature

Regarding temperature modelling, field sampling measurements were available in addition to the reference meteorological station data. This allowed us to train and use a machine learning technique (Random Forest). This powerful tool for topo-climatic forecast (Yoo et al. 2018; Bochenek and Ustrnul 2022), allowed us to predict air temperatures based on several topographic and climatic parameters (i.e., from DEM and reference station data inputs, respectively). For both minimum and maximum temperatures, models were trained to compute the difference between field sampling and station data. In both cases, the random forests models explained around 55-60% of variation in air temperatures.
These models could be further improved by increasing the sampling effort and capturing a larger diversity of topographic conditions, especially concerning the elevation range. Moreover, other influential parameters could be taken into account in order to explain more variation in temperatures, especially vegetation-related parameters. For instance, variations in normalized difference vegetation index and leaf area index (LAI) influence the variations and assessment of temperatures (Bennie et al. 2008; Kloog et al. 2017; Hough et al. 2020; Ahmed et al. 2024; Chang et al. 2024).
Due to the structure of the climate downscaling chain, improvements in minimum and maximum temperatures prediction would also improve the prediction of other parameters, namely mean air temperature and potential evapotranspiration. Indeed, mean air temperature has been computed as the arithmetic mean of minimum and maximum daily air temperatures. This simple and traditional method relies on the assumption that the daily temperature curve is symmetrical. In most cases, it is sufficient to approximate mean temperature. However, it has been shown to overestimate mean temperature in certain circumstances. Mean air temperature prediction could be improved using hourly temperatures (Bernhardt et al. 2018). If hourly temperature data are not available, the use of dynamic models accounting for temperature anomalies could also be explored (Tsonis et al. 2019).

Potential evapotranspiration

Because of the lack of knowledge of certain physics parameters in the case study (e.g., soil heat flux density and air resistance), potential evapotranspiration has been calculated through a simplified Priestley-Taylor method (Priestley and Taylor 1972; Allen et al. 1998). This model only requires global radiations, minimum and maximum temperatures.
If all necessary physical data were available, the assessment of potential evapotranspiration could be further refined either by using the Penman-Monteith method or by refining the Priestley-Taylor. Indeed, the latter method could be enhanced by computing the specific value of the Priestley-Taylor coefficient in the studied area. In the case study, a constant value was attributed to this coefficient (0.16). This value can however slightly vary depending on seasons, land cover, LAI or ventilation conditions (Wu et al. 2021; Nikolaou et al. 2023).

Precipitation

Finally, the downscaling of precipitation was performed on recorded historical data from SAFRAN (1990-2020) and simulated data from DRIAS (2021-2100), in order to go from an 8 km to a 100 m resolution grid. More precisely, we used the DRIAS data for the climate scenarios RCP 4.5 and RCP 8.5 and CNRM-ALADIN63 regional climate model.

Precipitation data were downscaled with a bilinear method, which is quite a simple widely used technique for downscaling daily data. Other statistical methods could be considered, such as inverse distance weight (i.e., giving more weight to nearby points and less to distant points), which has demonstrated good performance in rainfall interpolation (Ma et al. 2024). Compared to the bilinear method, inverse distance weighting is better suited to compute non-uniform grids, but it is also computationally more intensive than the bilinear method. In order to improve this step, other types of downscaling could have been employed, such as dynamic downscaling (i.e., simulating physical processes), machine learning downscaling (e.g., random forest, neural network or support vector machine), or a combination of both these approaches (Tolika et al. 2007; Wang et al. 2021; Yoshikane and Yoshimura 2023; Das et al. 2024). However, dynamic downscaling requires additional data that is not always easily available, especially at fine resolution. Moreover, machine learning requires a significant computational power, making statistical downscaling more energy-efficient, while remaining robust enough for daily precipitation data projections.

Potential application of topo-climatic downscaling: tree distribution projection

Remarkably, the topo-climatic downscaling chain developed in this study can be an upstream step for a species distribution model. For instance the distribution model Phenofit (Chuine and Beaubien 2001) requires daily minimum, maximum and mean temperatures, potential evapotranspiration and precipitation, which can all be estimated through our modelling pipeline. This process-based model simulates trees' phenological response to environmental conditions and predicts tree species potential distributions. It relies on the principle that the synchronization between the tree annual cycle and the seasonal variations of meteorological conditions strongly influences its adaptation to the environmental conditions (Chuine and Beaubien 2001; Morin and Chuine 2005). All functional traits simulated in the model thus vary with the pedoclimatic conditions. For that reason, this model also requires phenological data (e.g., dates of leaf colouring, leafing, flowering, fruiting, and temperatures of leaf and flower injuries), the elevation and the soil water holding capacity (see Appendix 3).

Conclusion

Climate modelling is a powerful tool for anticipating climate change and developing measures to deal with its consequences. There are many approaches to such a modelling, all with advantages and disadvantages in terms of necessary input data, prediction accuracy and robustness, time cost, and energy consumption.
The present study introduces a methodology to downscale at fine spatial resolution global solar radiations, temperatures (minimum, maximum and mean daily values), potential evapotranspiration and precipitation. These variables are computed through a modelling pipeline combining empirical and machine learning approaches. Machine learning models are some of the most powerful tools to accurately describe and predict the influence of topography on climatic variables. However, they need to be trained with a large amount of *in situ* data in order to be tailor-made to a given area. In this study, the daily field sampling conducted with 27 stations with data loggers during almost two years has enabled us to collect the necessary data for powerful modelling.

Topo-climatic predictions can be used to produce maps, which are great media for participatory research. Indeed, cartography provides concrete feedback and basis for making decisions, as it enables the visualization of the results and highlights the influence of topography on variables of great importance for agriculture (e.g., temperatures). In this specific case study, produced maps will be part of a decision-making tool developed in the context of the RESILIÂNCE project (resilience of fruit-producing chestnut tree orchards and innovation of cultivation techniques in the face of global changes). This project is funded by the French Ministry of Agriculture through the PARSADA program, which is a strategic action plan aiming to anticipate the potential European withdrawal of active substances and develop alternative crop protection techniques. The goal of this decision-making tool would be to help chestnut growers anticipate climate change in their specific geographical situation. This could contribute to the conservation effort of chestnut trees (namely local varieties that might be fitted to face harsh conditions), as well as the associated cultivation knowledge and practices.

Acknowledgments

We are thankful to the SNPC (*Syndicat National des Producteurs de Châtaignes*, National chestnut producers' union), ADEME (French national environmental transition agency) and to the Fondation de France for supporting the ROC-CHÂ project. We are also thankful to the members of the ROC-CHÂ collective for their involvement in the meteorological monitoring on field. We are grateful as well to Daphné Asse for the preliminary modelling work that paved the way to this study.

References

Ahmed, Ali Yasin, Abebe Mohammed Ali, and Nurhussen Ahmed. 2024. 'Temporal Dynamics of Leaf Area Index and Land Surface Temperature Correlation Using Sentinel-2 and Landsat OLI Data'. *Environmental Systems Research* 13 (1): 43. https://doi.org/10.1186/s40068-024-00371-6.

Allen, R.G., L.S. Pereira, D. Raes, and M. Smith. 1998. 'FAO Irrigation and Drainage Paper'. *FAO* 56: 300.

Álvarez-Álvarez, Pedro, Adrián Aviñoa-Arias, Emilio Díaz-Varela, José Vicente López-Bao, and José Carlos Pérez-Girón. 2025. 'Impact of Climate Change over Distribution and Potential Range of Chestnut in the Iberian Peninsula'. *Frontiers in Forests and Global Change* 8 (February): 1561027. https://doi.org/10.3389/ffgc.2025.1561027.

Anupoju, Varaprasad, Bvn P. Kambhammettu, and Srinivasa Rao Peddinti. 2024. 'Comparative Analysis of FAO Dual Kc, Priestley-Taylor and Flux Variance Similarity Methods in Partitioning Evapotranspiration from Flood-irrigated Rice Fields'. *Irrigation and Drainage*, September 30, ird.3039. https://doi.org/10.1002/ird.3039.

Aumeeruddy-Thomas, Y., N. Ponsa, E. Calvet, et al. 2024. 'Methodology for Phenoclimatic Observations and Modelling of *Castanea Sativa* Mill. Traditional Cultivars and Revitalizing Chestnut Growers' Local Knowledge in France, ROC-CHA Project'. *Acta Horticulturae*, no. 1400 (July): 31–40. https://doi.org/10.17660/actahortic.2024.1400.4.

Aumeeruddy-Thomas, Y., and A. Ramet. 2020. 'La Châtaigneraie Fruitière Cévenole : Un Agroécosystème Aux Multiples Valeurs Socio-Culturelles et Écosystémiques Face Au Changement Climatique'. In *Adaptation Du Parc National Des Cévennes Au Changement Climatique et à Ses Impacts*, Parc national des Cévennes. https://www.calameo.com/books/006434175254eafbd9d01.

Aumeeruddy-Thomas, Yildiz, Clara Therville, Cedric Lemarchand, Alban Lauriac, and Franck Richard. 2012. 'Resilience of Sweet Chestnut and Truffle Holm-Oak Rural Forests in Languedoc-Roussillon, France: Roles of Social-Ecological Legacies, Domestication, and Innovations'. *Ecology and Society* 17 (2). https://doi.org/10.5751/ES-04750-170212.

Baude, Manuel, Aurore Colin, Clara Calipel, Jérôme Duvernoy, and Alexis Foussard. 2022. *DataLab - Chiffres Clés Du Climat - France, Europe et Monde*. Ministère de la transition écologique & Service des données et études statistiques (SDES). http://www.statistiques.developpement-durable.gouv.fr.

Bennie, Jonathan, Brian Huntley, Andrew Wiltshire, Mark O. Hill, and Robert Baxter. 2008. 'Slope, Aspect and Climate: Spatially Explicit and Implicit Models of Topographic Microclimate in Chalk Grassland'. *Ecological Modelling* 216 (1): 47–59. https://doi.org/10.1016/j.ecolmodel.2008.04.010.

Bernhardt, Jase, Andrew M. Carleton, and Chris LaMagna. 2018. 'A Comparison of Daily Temperature-Averaging Methods: Spatial Variability and Recent Change for the CONUS'. *Journal of Climate* 31 (3): 979–96. https://doi.org/10.1175/JCLI-D-17-0089.1.

Bochenek, Bogdan, and Zbigniew Ustrnul. 2022. 'Machine Learning in Weather Prediction and Climate Analyses—Applications and Perspectives'. *Atmosphere* 13 (2): 180. https://doi.org/10.3390/atmos13020180.

Calvin, Katherine, Dipak Dasgupta, Gerhard Krinner, et al. 2023. *IPCC, 2023: Climate Change 2023: Synthesis Report. Contribution of Working Groups I, II and III to the Sixth Assessment Report of the Intergovernmental Panel on Climate Change [Core Writing Team, H. Lee and J. Romero (Eds.)]. IPCC, Geneva, Switzerland.* First. With Hoesung Lee. Intergovernmental Panel on Climate Change (IPCC). https://doi.org/10.59327/IPCC/AR6-9789291691647.

Chang, Hongfang, Jiabing Cai, Di Xu, Lei Jiang, Chunsheng Zhang, and Baozhong Zhang. 2024. 'Precision Modelling of Leaf Area Index for Enhanced Surface Temperature Partitioning and Improved

Evapotranspiration Estimation'. *Agricultural and Forest Meteorology* 356 (September): 110157. https://doi.org/10.1016/j.agrformet.2024.110157.

Chuine, Isabelle, and Elisabeth G. Beaubien. 2001. 'Phenology Is a Major Determinant of Tree Species Range'. *Ecology Letters* 4 (5): 500–510. https://doi.org/10.1046/j.1461-0248.2001.00261.x.

Das, Puja, August Posch, Nathan Barber, et al. 2024. 'Hybrid Physics-AI Outperforms Numerical Weather Prediction for Extreme Precipitation Nowcasting'. *Npj Climate and Atmospheric Science* 7 (1): 282. https://doi.org/10.1038/s41612-024-00834-8.

De Cáceres, Miquel, Nicolas Martin-StPaul, Marco Turco, Antoine Cabon, and Victor Granda. 2018. 'Estimating Daily Meteorological Data and Downscaling Climate Models over Landscapes'. *Environmental Modelling & Software* 108 (October): 186–96. https://doi.org/10.1016/j.envsoft.2018.08.003.

Decharme, Bertrand, Christine Delire, Marie Minvielle, et al. 2019. 'Recent Changes in the ISBA-CTRIP Land Surface System for Use in the CNRM-CM6 Climate Model and in Global Off-Line Hydrological Applications'. *Journal of Advances in Modeling Earth Systems* 11 (5): 1207–52. https://doi.org/10.1029/2018MS001545.

Druel, Arsène, Julien Ruffault, Hendrik Davi, et al. 2025. 'Enhancing Environmental Models with a New Downscaling Method for Global Radiation in Complex Terrain'. *Biogeosciences* 22 (1): 1–18. https://doi.org/10.5194/bg-22-1-2025.

Durand, Y., E. Brun, L. Merindol, G. Guyomarc'h, B. Lesaffre, and E. Martin. 1993. 'A Meteorological Estimation of Relevant Parameters for Snow Models'. *Annals of Glaciology* 18: 65–71. https://doi.org/10.3189/S0260305500011277.

Freitas, Teresa R., João A. Santos, Ana P. Silva, and Hélder Fraga. 2021. 'Influence of Climate Change on Chestnut Trees: A Review'. *Plants* 10 (7): 1463. https://doi.org/10.3390/plants10071463.

Friedberg, Rina, Julie Tibshirani, Susan Athey, and Stefan Wager. 2021. 'Local Linear Forests'. *Journal of Computational and Graphical Statistics* 30 (2): 503–17. https://doi.org/10.1080/10618600.2020.1831930.

George H. Hargreaves and Zohrab A. Samani. 1985. 'Reference Crop Evapotranspiration from Temperature'. *Applied Engineering in Agriculture* 1 (2): 96–99. https://doi.org/10.13031/2013.26773.

Gürel, Ali Etem, Ümit Ağbulut, Hüseyin Bakır, Alper Ergün, and Gökhan Yıldız. 2023. 'A State of Art Review on Estimation of Solar Radiation with Various Models'. *Heliyon* 9 (2): e13167. https://doi.org/10.1016/j.heliyon.2023.e13167.

HEC-HMS Technical Reference Manual. n.d. https://www.hec.usace.army.mil/.

Hough, Ian, Allan C. Just, Bin Zhou, Michael Dorman, Johanna Lepeule, and Itai Kloog. 2020. 'A Multi-Resolution Air Temperature Model for France from MODIS and Landsat Thermal Data'. *Environmental Research* 183 (April): 109244. https://doi.org/10.1016/j.envres.2020.109244.

Jacob, Daniela, Claas Teichmann, Stefan Sobolowski, et al. 2020. 'Regional Climate Downscaling over Europe: Perspectives from the EURO-CORDEX Community'. *Regional Environmental Change* 20 (2). https://doi.org/10.1007/s10113-020-01606-9.

Kloog, Itai, Francesco Nordio, Johanna Lepeule, et al. 2017. 'Modelling Spatio-Temporally Resolved Air Temperature across the Complex Geo-Climate Area of France Using Satellite-Derived Land Surface Temperature Data: MODELLING AIR TEMPERATURE IN FRANCE'. *International Journal of Climatology* 37 (1): 296–304. https://doi.org/10.1002/joc.4705.

Kumar, Lalit, Andrew K. Skidmore, and Edmund Knowles. 1997. 'Modelling Topographic Variation in Solar Radiation in a GIS Environment'. *International Journal of Geographical Information Science* 11 (5): 475–97. https://doi.org/10.1080/136588197242266.

Lembrechts, Jonas J., Ivan Nijs, and Jonathan Lenoir. 2019. ‘Incorporating Microclimate into Species Distribution Models’. *Ecography* 42 (7): 1267–79. https://doi.org/10.1111/ecog.03947.

Ma, Qiang, Siyuan Chang, Guowei Lu, and Philippe Gourbesville. 2024. ‘Assessment of Different Interpolation Algorithms for Daily Rainfall Spatial Distribution in the Var Catchment, France’. *River* 3 (4): 362–72. https://doi.org/10.1002/rvr2.106.

Michelangeli, P.-A., M. Vrac, and H. Loukos. 2009. ‘Probabilistic Downscaling Approaches: Application to Wind Cumulative Distribution Functions’. *Geophysical Research Letters* 36 (11). https://doi.org/10.1029/2009gl038401.

Morin, Xavier, and Isabelle Chuine. 2005. ‘Sensitivity Analysis of the Tree Distribution Model PHENOFITto Climatic Input Characteristics: Implications for Climate Impact Assessment’. *Global Change Biology* 11 (9): 1493–503. https://doi.org/10.1111/j.1365-2486.2005.00996.x.

Nabat, Pierre, Samuel Somot, Christophe Cassou, et al. 2020. ‘Modulation of Radiative Aerosols Effects by Atmospheric Circulation over the Euro-Mediterranean Region’. *Atmospheric Chemistry and Physics* 20 (14): 8315–49. https://doi.org/10.5194/acp-20-8315-2020.

Nabat, Pierre, Samuel Somot, Marc Mallet, Arturo Sanchez-Lorenzo, and Martin Wild. 2014. ‘Contribution of Anthropogenic Sulfate Aerosols to the Changing Euro-Mediterranean Climate since 1980’. *Geophysical Research Letters* 41 (15): 5605–11. https://doi.org/10.1002/2014gl060798.

Nikolaou, Georgios, Damianos Neocleous, Evangelini Kitta, and Nikolaos Katsoulas. 2023. ‘Assessment of the Priestley-Taylor Coefficient and a Modified Potential Evapotranspiration Model’. *Smart Agricultural Technology* 3 (February): 100075. https://doi.org/10.1016/j.atech.2022.100075.

Piedallu, Christian, and Jean-claude Gégout. 2008. ‘Efficient Assessment of Topographic Solar Radiation to Improve Plant Distribution Models’. *Agricultural and Forest Meteorology* 148 (11): 1696–706. https://doi.org/10.1016/j.agrformet.2008.06.001.

Priestley, C. H. B., and R. J. Taylor. 1972. ‘On the Assessment of Surface Heat Flux and Evaporation Using Large-Scale Parameters’. *Monthly Weather Review* 100 (2): 81–92. https://doi.org/10.1175/1520-0493(1972)100<0081:OTAOSH>2.3.CO;2.

Riahi, Keywan, Shilpa Rao, Volker Krey, et al. 2011. ‘RCP 8.5—A Scenario of Comparatively High Greenhouse Gas Emissions’. *Climatic Change* 109 (1–2): 33–57. https://doi.org/10.1007/s10584-011-0149-y.

Rigatti, Steven J. 2017. ‘Random Forest’. *Journal of Insurance Medicine* 47 (1): 31–39. https://doi.org/10.17849/insm-47-01-31-39.1.

Rita, Angelo, Giuliano Bonanomi, Emilia Allevato, et al. 2021. ‘Topography Modulates Near-Ground Microclimate in the Mediterranean Fagus Sylvatica Treeline’. *Scientific Reports* 11 (1): 8122. https://doi.org/10.1038/s41598-021-87661-6.

Robin, Y., L. Corre, P. Marson, S. Bernu, M. Vrac, and S. Thao. 2023. *Projections Climatiques Régionalisées : Correction de Biais et Changements Futurs. Projet Explore2 : Anticiper Les Évolutions Climatiques et Hydrologiques En France*.

Roderick, Michael L. 1999. ‘Estimating the Diffuse Component from Daily and Monthly Measurements of Global Radiation’. *Agricultural and Forest Meteorology* 95 (3): 169–85. https://doi.org/10.1016/S0168-1923(99)00028-3.

Rolnick, David, Priya L. Donti, Lynn H. Kaack, et al. 2023. ‘Tackling Climate Change with Machine Learning’. *ACM Computing Surveys* 55 (2): 1–96. https://doi.org/10.1145/3485128.

Sekulić, Aleksandar, Milan Kilibarda, Gerard B.M. Heuvelink, Mladen Nikolić, and Branislav Bajat. 2020. ‘Random Forest Spatial Interpolation’. *Remote Sensing* 12 (10): 1687. https://doi.org/10.3390/rs12101687.

Thomson, Allison M., Katherine V. Calvin, Steven J. Smith, et al. 2011. 'RCP4.5: A Pathway for Stabilization of Radiative Forcing by 2100'. *Climatic Change* 109 (1–2): 77–94. https://doi.org/10.1007/s10584-011-0151-4.

Tolika, Konstantia, Panagiotis Maheras, Margaritis Vafiadis, and Christina Anagnostopoulou. 2007. 'Comparaison de Deux Scénarios (Statistique et Dynamique) Concernant Les Précipitations Hivernales En Grèce'. *Climatologie* 4: 73–90. https://doi.org/10.4267/climatologie.726.

Tsonis, Anastasios A., Xinnong Pan, Geli Wang, and Catherine Nicolis. 2019. 'On the Min–Max Estimation of Mean Daily Temperatures'. *Climate Dynamics* 53 (3–4): 1981–89. https://doi.org/10.1007/s00382-019-04757-6.

Van Der Meersch, Victor, Edward Armstrong, Florent Mouillot, et al. 2024. 'Biological Mechanisms Are Necessary to Improve Projections of Species Range Shifts'. Preprint, Cold Spring Harbor Laboratory, May 8. https://doi.org/10.1101/2024.05.06.592679.

Vautard, Robert, Nikolay Kadygrov, Carley Iles, et al. 2021. 'Evaluation of the Large EURO-CORDEX Regional Climate Model Ensemble'. *Journal of Geophysical Research: Atmospheres* 126 (17). https://doi.org/10.1029/2019jd032344.

Verfaillie, Deborah, Michel Déqué, Samuel Morin, and Matthieu Lafaysse. 2017. 'The Method ADAMONT v1.0 for Statistical Adjustment of Climate Projections Applicable to Energy Balance Land Surface Models'. *Geoscientific Model Development* 10 (11): 4257–83. https://doi.org/10.5194/gmd-10-4257-2017.

Vrac, Mathieu. 2018. 'Multivariate Bias Adjustment of High-Dimensional Climate Simulations: The Rank Resampling for Distributions and Dependences (R^2D^2) Bias Correction'. *Hydrology and Earth System Sciences* 22 (6): 3175–96. https://doi.org/10.5194/hess-22-3175-2018.

Vrac, Mathieu, and Soulivanh Thao. 2020. 'R^2D^2 v2.0: Accounting for Temporal Dependences in Multivariate Bias Correction via Analogue Rank Resampling'. *Geoscientific Model Development* 13 (11): 5367–87. https://doi.org/10.5194/gmd-13-5367-2020.

Wang, Jiali, Zhengchun Liu, Ian Foster, Won Chang, Rajkumar Kettimuthu, and V. Rao Kotamarthi. 2021. 'Fast and Accurate Learned Multiresolution Dynamical Downscaling for Precipitation'. *Geoscientific Model Development* 14 (10): 6355–72. https://doi.org/10.5194/gmd-14-6355-2021.

Wu, Hantian, Weiwei Zhu, and Bo Huang. 2021. 'Seasonal Variation of Evapotranspiration, Priestley-Taylor Coefficient and Crop Coefficient in Diverse Landscapes'. *Geography and Sustainability* 2 (3): 224–33. https://doi.org/10.1016/j.geosus.2021.09.002.

Yoo, Cheolhee, Jungho Im, Seonyoung Park, and Lindi J. Quackenbush. 2018. 'Estimation of Daily Maximum and Minimum Air Temperatures in Urban Landscapes Using MODIS Time Series Satellite Data'. *ISPRS Journal of Photogrammetry and Remote Sensing* 137 (March): 149–62. https://doi.org/10.1016/j.isprsjprs.2018.01.018.

Yoshikane, Takao, and Kei Yoshimura. 2023. 'A Downscaling and Bias Correction Method for Climate Model Ensemble Simulations of Local-Scale Hourly Precipitation'. *Scientific Reports* 13 (1): 9412. https://doi.org/10.1038/s41598-023-36489-3.

Appendix

Appendix 1: Maps of the studied area, with a) ESRI satellite view and b) digital elevation model (100 m resolution)

The border between the Departments of Lozère and Gard is represented by a dashed line and the name of the main places are indicated (with the Cévennes National Park in green).

a)

b)

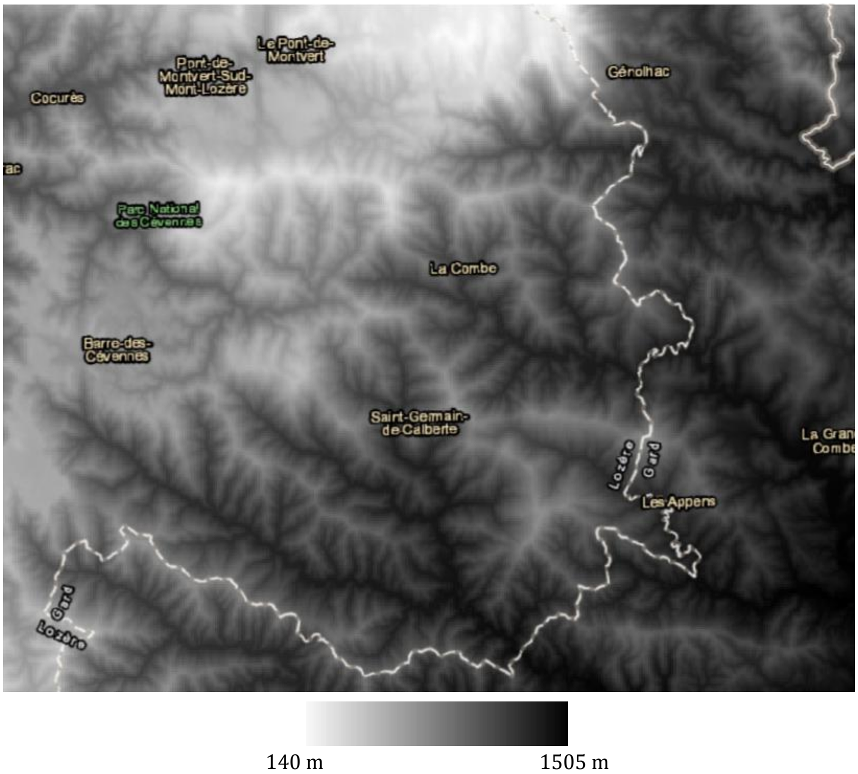

<u>Appendix 2</u>: RStudio packages used in the modelling pipeline

Package name	Package use	Modelled variables
data.table	Fast aggregation of large data, fast ordered joins, fast add/modify/delete of columns by group using no copies at all, list columns, friendly and fast character-separated-value read/write.	water holding capacity
dplyr	Data common manipulation	water holding capacity
grf	Forest-based statistical estimation and inference	temperatures
insol[1]	Computing radiations parameters	radiations
rgdal[2]	Handling geospatial data	radiations and temperatures
oce	Estimating atmospheric pressure	radiations
plotmo	Plot a Model's Residuals, Response, and Partial Dependence Plots	temperatures
randomForest	Implementations for Breiman and Cutlers Random Forests for Classification and Regression	temperatures
raster	Reading, writing, manipulating, analyzing and modelling of spatial data	radiations, temperatures, potential evapotranspiration, precipitation and water holding capacity
RAtmosphere[3]	Modelling atmospheric parameters as a function of elevation and climatic parameters	radiations
ROCR	Evaluating and visualizing the performance of scoring classifiers	temperatures
terra	Spatial data analysis with vector (points, lines, polygons) and raster (grid) data.	water holding capacity
tidyr	Tools to help to create tidy data	water holding capacity

[1] The package has been archived but it can still be downloaded from for manual installation (https://cran.r-project.org/package=insol).
[2] The package has been archived but it can still be downloaded from for manual installation (https://cran.r-project.org/package=rgdal).
[3] The package has been archived but it can still be downloaded from for manual installation (https://cran.r-project.org/package=RAtmosphere).

Appendix 3: Water holding capacity modelling

The **water holding capacity (*WHC*) in mm** corresponds to the maximum quantity of water that the soil is able to retain against gravity after saturation and drainage. It depends on a number of factors such as soil depth, texture and structure. For instance, clay soils retain more water than sandy soils and a good structure favours retention (Bronick & Lal 2005; Wankmüller et al., 2024). Furthermore, the presence of coarse fragments and a low depth to the bedrock reduces water storage space (Baetens et al., 2009; Sekucia et al., 2020). WHC was computed using **water content at field capacity and at wilting point** (i.e., the percentage of bulk water content retained by the soil at −33 kPa and −1,500 kPa pressure, respectively) retrieved from *EU Soil Hydraulic Grid 1km*[4], and **depth to bedrock and coarse fragment data** retrieved from *Soil Grid 2.0 250m*[5]. Both grids describe **the first two meters of soil, separated into six layers**: 0–5 cm, 5–15 cm, 15–30 cm, 30–60 cm, 60–100 cm and 100-200 cm (i.e., with respective theoretical thickness of 5, 10, 15, 30, 40 and 100 cm, see Figure 12).

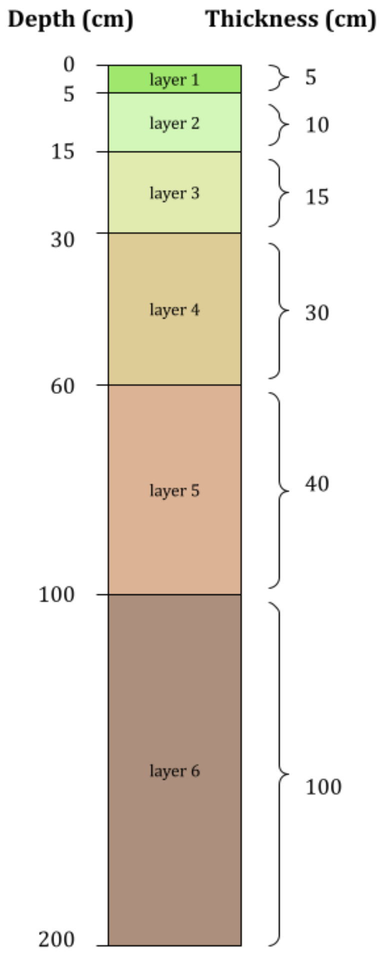

Figure 12: Depths and thicknesses of soil layers.

All the input grid data are first **downscaled** with the raster::resample() function, using the DEM as reference. Then, **the moving average value of water capacities and coarse fragment** are

[4] 3D Soil Hydraulic Database of Europe at 1 km and 250 m resolution - ESDAC - European Commission
[5] SoilGrids250m 2.0

computed for each layer. That way, instead of using their values at all seven initial depths separately, the mean value between consecutive layers is considered. This approach allows a smoother transition between depths while maintaining a representative value for each soil layer.
Finally, for each layer, the WHC is calculated based on the **difference between the water content at field capacity and at wilting point**. This difference is then weighted with the **volumetric percentage of coarse fragments** and the actual **thickness of the layer**, which takes into account the depth to bedrock. Indeed, the thickness of the layer is reduced if the bedrock is reached before the maximum theoretical depth of that layer (e.g., if the bedrock is reached at 120cm, then layer 6 ends at 120cm and not 200cm). The total soil WHC of the two first meters (divided *n* layers of soil) is thus obtained as follows (Toth et al., 2017):

$$WHC = \sum_{k=1}^{n} \frac{WC^{FC} - WC^{WP}}{100} * \frac{100 - CF_k}{100} * th_k$$

<u>Table 8</u>: Parameters used in the WHC formula

Symbol	Parameter	Value or equation	Unit
CF	volumetric percentage of coarse fragment (>2mm)	*from Soil Grid 2.0 250m*	%
$depth^{BR}$	soil depth to bedrock	*from Soil Grid 2.0 250m*	cm
$depth_k$	maximum depth of layer k	5, 15, 30, 60, 100 and 200	cm
k	current layer of soil layer	*1 to n*	/
n	total number of soil layers	6	/

th_k	layer thickness corrected coefficient	if $depth^{BR} \geq depth_k$:
		$th_k = th_k^{theoritical}$
		
		if $depth^{BR} < depth_k$:
		$th_k = \max(0, depth^{BR} - depth_k)$
			cm

$th_k^{theoritical}$	thickness based solely on the *k* layer's depth	5, 10, 15, 30, 40 and 100	cm
WC^{FC}	water content at field capacity	*from EU Soil Hydro Grid 1km*	%
WC^{WP}	water content at wilting point	*from EU Soil Hydro Grid 1km*	%